International Journal of Nanomedicine

Dovepress
Taylor & Francis Group

Open Access Full Text Article

ORIGINAL RESEARCH

Novel Antigen-Presenting Cell-Targeted Nanoparticles Enhance Split Vaccine Immunity Through Microneedles Inoculation

Xueliang Xiu[1,*], Hongyang Fu[2,*], Ruipeng Zhang[3], Shichao Ma[1], Panpan Guo[1], Zhipeng Li[1], Yihan Zhu[4], Fengsen Ma[1,5,6]

[1]College of Pharmacy, Zhejiang University of Technology, Deqing, 313216, People's Republic of China; [2]Department of Dermatology, The First Affiliated Hospital of Zhejiang Chinese Medical University (Zhejiang Provincial Hospital of Chinese Medicine), Hangzhou, 310006, People's Republic of China; [3]Emergency Department, Beijing Tiantan Hospital, Capital Medical University, Beijing, 100070, People's Republic of China; [4]State Key Laboratory of Green Technologies for Chemical Synthesis and Conversion, College of Chemical Engineering, Zhejiang University of Technology, Hangzhou, 310014, People's Republic of China; [5]Micro-nano Scale Biomedical Engineering Laboratory, Institute for Frontiers and Interdisciplinary Sciences, Zhejiang University of Technology, Hangzhou, 310014, People's Republic of China; [6]Zhejiang Provincial Key Laboratory of Quantum Precision Measurement, Hangzhou, 310023, People's Republic of China

*These authors contributed equally to this work

Correspondence: Yihan Zhu, State Key Laboratory of Green Technologies for Chemical Synthesis and Conversion, College of Chemical Engineering, Zhejiang University of Technology, Hangzhou, 310014, People's Republic of China, Tel/Fax +86 571 88320178, Email yihanzhu@zjut.edu.cn; Fengsen Ma, Micro-nano Scale Biomedical Engineering Laboratory, Institute for Frontiers and Interdisciplinary Sciences, Zhejiang University of Technology, Hangzhou, 310014, People's Republic of China, Tel/Fax +86 571 88320218, Email sunny@zjut.edu.cn

Aim/Background: Despite their superior safety and widespread use, split vaccines typically suffer from reduced immunogenicity due to the lack of an intact viral structure. Targeting the mannose receptors on antigen-presenting cells (APCs) with nanoparticles (NPs) and delivering them via microneedles (MNs) offers a promising solution. We designed and synthesized NPs that could form complexes with split H1N1 antigens, and evaluated the immunogenicity after loading them into dissolvable microneedle arrays (dMAs).

Methods: Man-N-HACC was synthesized by conjugating mannose moieties to N-2-hydroxypropyl trimethyl ammonium chloride chitosan (N-HACC), followed by cross-linking with tripolyphosphate to form Man-N-HACC NPs. The NPs were characterized in terms of morphology, size, zeta potential, spatial orientation, macrophage internalization, and stability. The microstructure, mechanical strength, skin penetration capability, and release behavior of dMAs loaded with Man-N-HACC NPs/H1N1 complexes were investigated. Finally, the efficacy of dMAs was assessed in a rat model using ELISA and hemagglutination inhibition (HAI) assay.

Results: Characterization via Fourier transform infrared spectroscopy and nuclear magnetic resonance confirmed the synthesis of Man-N-HACC. The cross-linked generated Man-N-HACC NPs displayed uniform morphology and good stability over 28 days, along with confirmed spatial orientation of mannose ligands and macrophage internalization. The dMAs loaded with Man-N-HACC NPs/H1N1 exhibited mechanical robustness, capable of fully penetrating the skin and releasing nanovaccines. The increase in HAI titers and total IgG antibody levels in rat serum indicates the effectiveness of humoral immunity, and this effect only occurs after NPs formed post-crosslinking, rather than directly using raw nanomaterials, highlighting the critical role of the nanoparticle structure.

Conclusion: This study confirms that the delivery of Man-N-HACC NPs via dMAs provides a novel and promising approach for the administration of split influenza vaccines. Moreover, it underscores the great potential of nano-adjuvants in enhancing the efficacy of split vaccines.

Keywords: mannose receptor, target, nanoparticles, dissolvable microneedle arrays, split vaccine

Introduction

Numerous studies have demonstrated that vaccination can effectively reduce both infection and mortality rates. Although the global outbreak of COVID-19 has been brought under control, the spread of influenza viruses continues to pose a persistent threat to global health.[1] Many individuals still refuse or delay vaccination due to the temporary discomfort

Received: 13 November 2024
Accepted: 22 March 2025
Published: 30 April 2025

Graphical Abstract

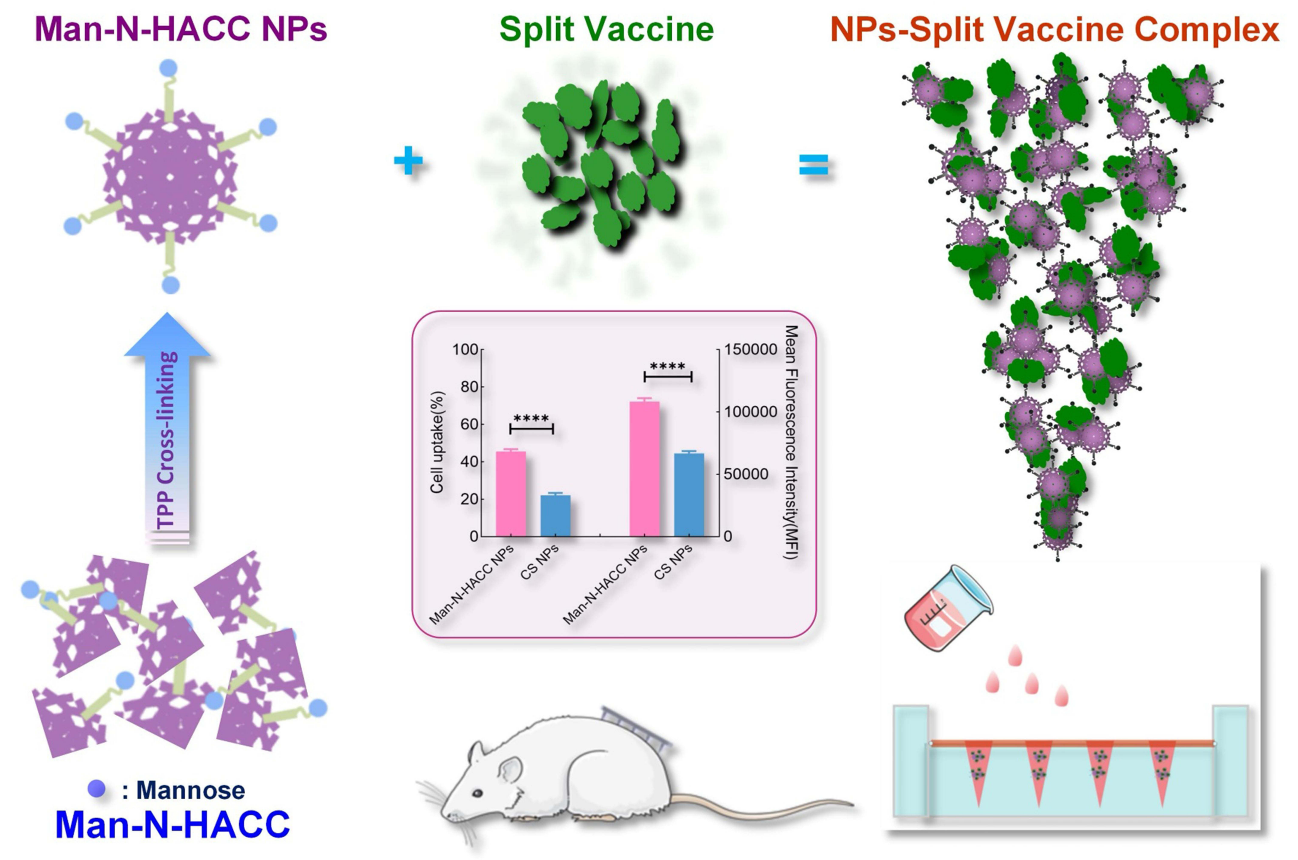

associated with traditional invasive methods such as intramuscular injections, which can cause pain and the risk of needlestick injuries.[2] In recent years, microneedles (MNs), a novel transdermal drug delivery technology has emerged as a minimally invasive alternative for percutaneous immunization, offering less pain and better compliance.[3] MNs can accurately deliver vaccines to the epidermis and dermis, thereby enhancing skin immune responses.[4,5] As a painless alternative to traditional vaccination strategies, MNs offer significant advantages in terms of immune effectiveness, vaccine stability, and dose sparing, making them a promising approach for expanding global influenza vaccination coverage.[6,7]

Currently, there are three types of influenza vaccines used clinically: inactivated vaccines (whole-virus vaccines, subunit vaccines, and split vaccines), live attenuated vaccines, and recombinant vaccines.[8] Although live attenuated vaccines can induce strong and long-lasting immune responses, they may lead to virus replication in immunocompromised individuals, causing severe side effects such as fever, syncope, and headache. Therefore, they are only approved for use in individuals aged 2 to 49 with normal immune system function.[9,10] The split vaccines have fewer side effects and are relatively simple to produce, making them a commonly used type of influenza vaccine. However, due to the lack of an intact virus structure, their immunogenicity is relatively weak, and it is difficult to induce immune responses comparable to those of live attenuated vaccines.[11] Therefore, powerful adjuvants are often required when delivering split vaccines using dissolvable microneedle arrays.[4,5]

The length of MNs, which is in the range of hundreds of micrometers, is highly conducive to precisely delivering vaccine particles into the skin to achieve effective transdermal immunization. Meanwhile, a microneedle arrays patch can fully enable simultaneous multi-point administration to generate multi-point stimulation, thereby enhancing the immunization effect. The combination of nanoparticles (NPs) with rapidly dissolving microneedles for antigen delivery has only been explored in the past few years. This combination may synergistically address the challenges of transdermal delivery of vaccines with inadequate delivery efficiency and or low immunogenicity. NPs have been recognized as a strategy to enhance immunogenicity, serving as immune adjuvants in vaccine formulations.[12,13] They can enhance the uptake and presentation of antigens by antigen presenting cells (APCs), stimulate the activation of immune cells, and regulate the secretion of cytokines. Additionally, NPs protect antigens from degradation, thereby enhancing vaccine efficacy.[14] The various receptors on the surface of antigen-presenting cells, such as Toll-like receptors (TLRs), C-type lectin receptors (CLRs),[15] provide inspiration for the targeted delivery of antigens and the enhancement of immune responses. Notably, mannose receptors (MRs), a type of CLRs, are widely distributed on the surface of macrophages and dendritic cells. They possess extracellular carbohydrate recognition domains (CRDs) that can bind to mannose-containing glycoconjugates.[15] MRs are highly efficient endocytic receptors, and the phagocytosis generated by the activation of their ligand binding creates favorable conditions for the uptake of vaccine antigens by APCs. Therefore, the grafting of mannose onto the surface of NPs is not only necessary but also a simple and effective strategy for achieving APC-targeted delivery and cross-presentation. This approach has the potential to significantly improve the immunogenicity and effectiveness of vaccine delivery systems, making them more effective in preventing and treating infectious diseases.

In this study, mannose moieties, which specifically bind to the MR on the surface of APCs, were conjugated to the amino groups of N-2-hydroxypropyl trimethyl ammonium chloride chitosan (N-HACC) molecules to form Man-N-HACC. NPs were then prepared from this material. To create the Man-N-HACC NPs, chitosan (CS), a cationic polysaccharide polymer, was quaternized to improve its water solubility. Subsequently, mannose molecules were grafted onto the modified CS. Tripolyphosphate (TPP) crosslinking was then employed to produce Man-N-HACC NPs. By interacting with influenza antigen, the Man-N-HACC NPs/H1N1 nano-vaccine was obtained. The dMAs were then loaded with the Man-N-HACC NPs/H1N1 to create a novel vaccine delivery platform, with a hypothesized immune mechanism in Figure 1. A systematic study was conducted on the morphology, physicochemical properties, insertion, and dissolution of the dMAs. Finally, the dMAs based on Man-N-HACC NPs was subjected to an in vivo investigation to verify whether it could induce a strong humoral immune response. Overall, it is expected that this proof-of-concept engineering exploration would provide an effective delivery strategy for split influenza vaccines, thereby facilitating the clinical development of other types of subunit vaccines and promote innovation and translation in microneedle-mediated vaccination.

Materials and Methods

Materials and Animals

The influenza antigen, influenza antigen standards and anti-influenza virus immune sera were kindly provided by Liaoning Chengda Biotechnology Co. Ltd. Bovine serum albumin (BSA) and bovine serum albumin-fluorescein isothiocyanate (BSA-FITC) were purchased from Beijing Solarbio Science & Technology Co. Ltd. Polyphosphoric acid sodium (TPP), Sodium cyanoborohydride ($NaBH_3CN$), glycidyl trimethylammonium chloride (GTMAC), cellulose acetate (CA), and rhodamine B were purchased from Shanghai Macklin Biochemical Technology Co. Ltd. Carboxymethyl cellulose (CMC) was purchased from Sinopharm Chemical Reagent Co. Ltd. Polyvinylpyrrolidone (PVP K90) was purchased from Guangdong Yuemei Chemical Co. Ltd. D-mannose, Coomassie Brilliant Blue (G250), poloxamer 188, acetic acid were purchased from Hangzhou Jigong Biotechnology Co. Ltd. N,N-dimethylformamide (DMF) was purchased from Shanghai Loen Chemical Technology Co. Ltd. Agarose (Low EEO) was purchased from Beyotime Biotechnology. Sodium chloride was purchased from Guangdong Guanghua Sci-Tech Co. Ltd. Methanol and acetone were purchased from Shanghai Titan Scientific Co. Ltd. Methylene blue was purchased from Shanghai Sanaisi Reagent Co. Ltd. PDMS and PDMS curing agent were purchased from Dow Corning Corporation. Chitosan (Mw = 50 kDa, 95% deacetylation) was purchased from Zhejiang Jinke Biochemical Co. Ltd. Depilatory cream was purchased from Reckitt Benckiser Home Hygiene (China) Ltd. Polyinosinic-polycytidylic acid (poly(I:C)) was purchased from Meiya Pharmaceutical Haian Co. Ltd (China). Rat alveolar macrophages (NR8383) and Ham's F-12 K Medium were

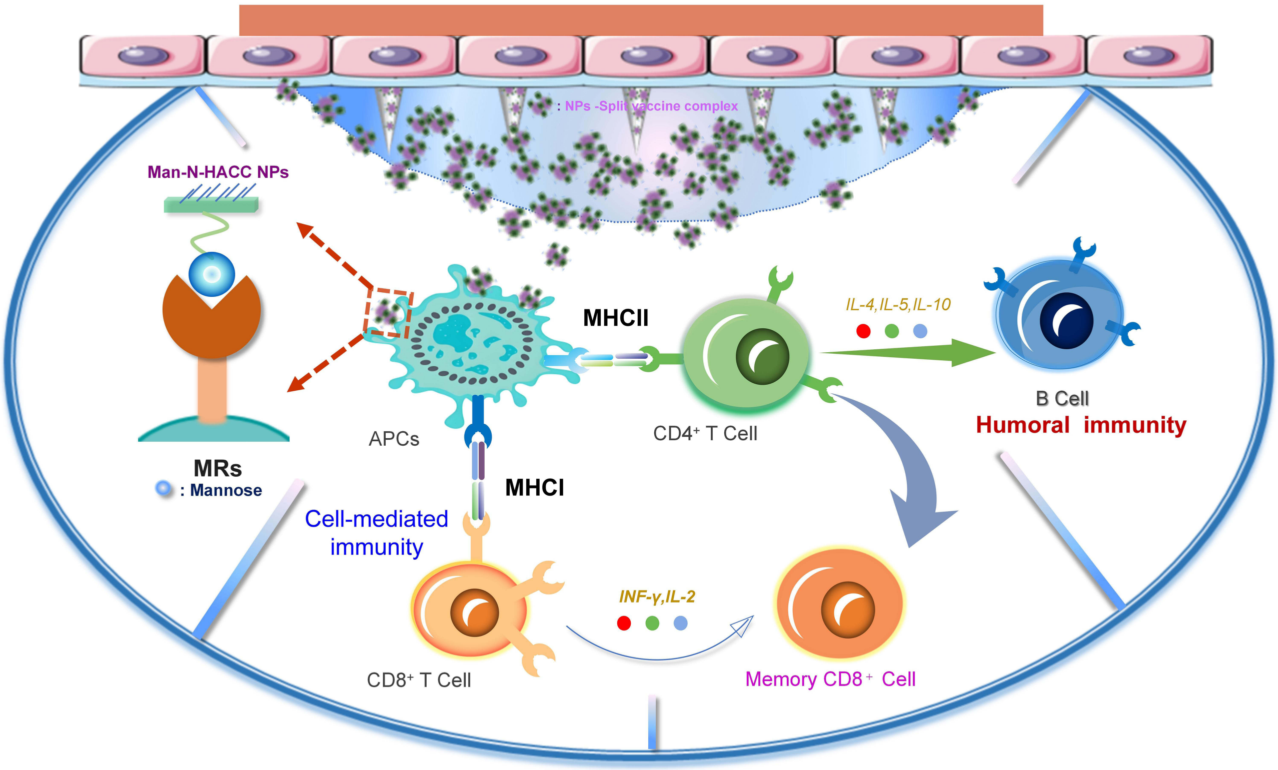

Figure 1 Schematic representation of the immunization mechanism of dMAs patch loaded with Man-N-HACC NPs/H1N1. The NPs-split vaccine complex is released from the microneedle, and the mannose moiety on the surface of its NPs are specifically recognized and bound by the mannose receptor of APCs, generating endocytosis of the cell, which allows the vaccine particles to enter the cell and be processed and presented, resulting in a series of immune responses.

purchased from National Collection of Authenticated Cell Cultures (China). Wistar rats (6 weeks old, male) were purchased from Zhejiang Vital River Laboratory Animal Technology Co. Ltd.

Synthesis and Characterization of Man-N-HACC

1.0 g of CS was dissolved in 200 mL of 5% (v/v) acetic acid (AcOH) solution and stirred overnight at room temperature until it became clear and transparent. Excessive glycidyl trimethylammonium chloride (GTMAC) was slowly added to the clear and transparent chitosan solution with a molar ratio of 1:1 to 1:3. The mixed solution was then stirred at 55 °C for 24 h. The mixture was centrifuged, and insoluble substances were removed by filtration. The clear solution was gradually added dropwise to 300 mL of pre-cooled acetone/ethanol (1:1, v/v) solution to obtain a precipitate. The precipitate was redissolved in a small amount of deionized water, and placed in a dialysis bag for 24 h. After dialysis, freeze-drying was performed to obtain N-HACC (Figure 2A). N-HACC was then subjected to Fourier Transform Infrared Spectroscopy (FTIR) and Nuclear Magnetic Resonance (NMR) ^{1}H spectroscopy for detection, and the degree of quaternization (DQ) was calculated according to formula (1). Elemental analyses of N-HACC and Man-N-HACC were performed on dried samples by an elemental analyzer (Elementar UNICUBE). The percentage of every element (C, H, and N) was used to calculate the degree of substitution of D-mannose on Man-N-HACC using formula (2).

$$DQ(\%) = \left[\frac{[(CH_3)_3]}{[H]} \times \frac{1}{9}\right] \times 100\% \tag{1}$$

$[(CH_3)_3]$: the peak area of the methyl proton peak in the quaternary ammonium salt. [H]: the peak area of the primary -CH- proton peak.

$$DS(\%) = \left[\frac{(C/N)_{Man-N-HACC} - (C/N)_{N-HACC}}{n}\right] \tag{2}$$

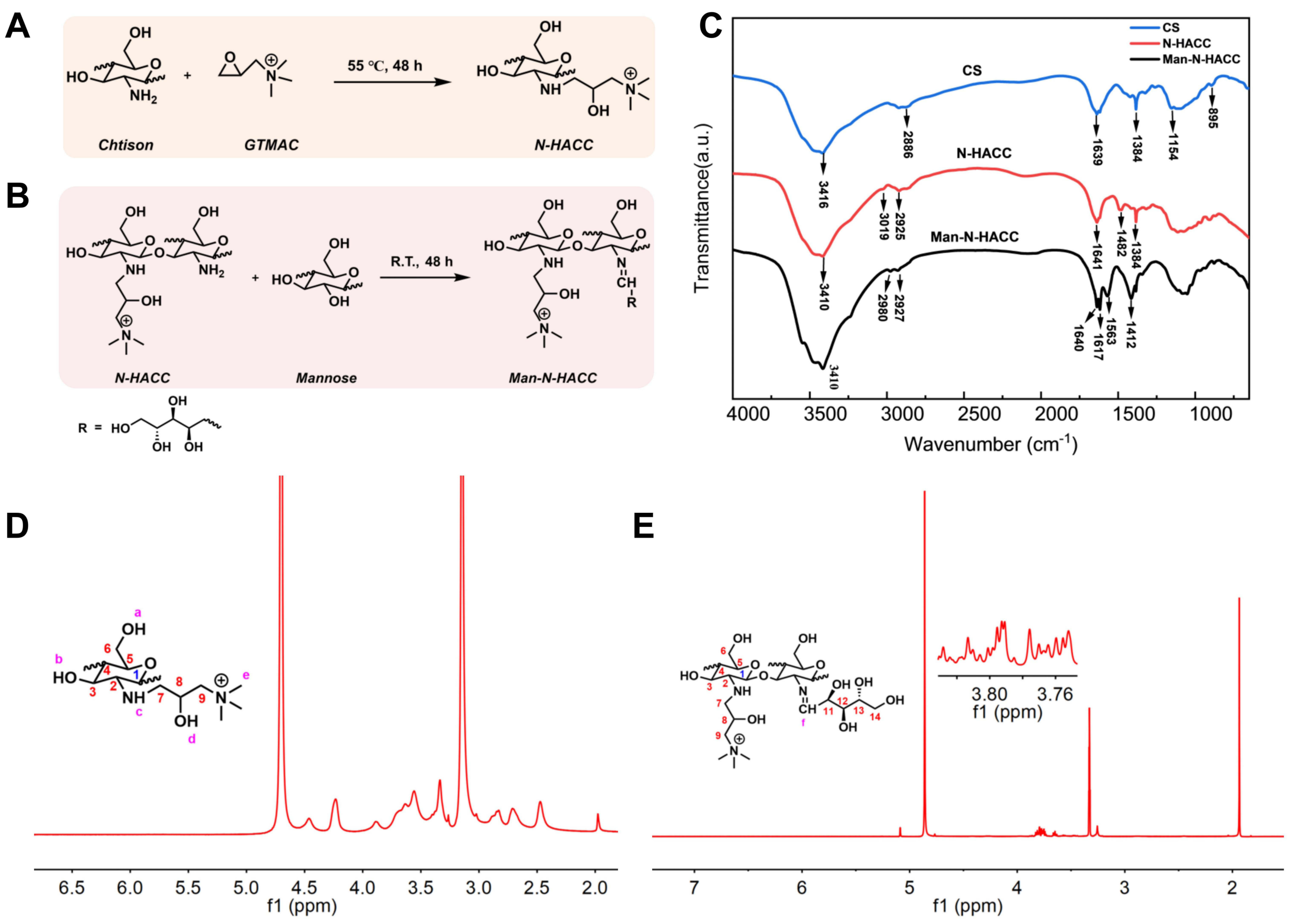

Figure 2 Synthesis and characterization of Man-N-HACC. (**A**) Synthesis route of N-HACC. GTMAC: glycidyl trimethylammonium chloride, N-HACC: N-2-hydroxypropyl trimethyl ammonium chloride chitosan. (**B**) Synthesis route of Man-N-HACC. R.T.: rotation. (**C**) FTIR spectra of CS, N-HACC, and Man-N-HACC. (**D**) ^{1}H NMR spectra of N-HACC. (**E**) ^{1}H NMR spectra of Man-N-HACC.

$(C/N)_{\text{Man-N-HACC}}$ is the C/N (element content ratios) of Man-N-HACC. $(C/N)_{\text{N-HACC}}$ is the C/N (element content ratios) of N-HACC. n is the atomicity of carbon of substituted unit.

0.50 g of D-mannose (D-Man) and 0.30 g of N-HACC were accurately weighed and dissolved in 100 mL of deionized water. 1.0 g of sodium cyanoborohydride ($NaBH_3CN$) was then added to the mixed solution, and stirred at room temperature for 48~72 h. A 2 M NaOH/absolute ethanol solution (1:1, v/v) was gradually added to the reaction mixture to purify the target product. A white gel-like precipitate was obtained after filtration, and redissolved in deionized water, then dialyzed for 24 h. Finally, freeze-drying was performed to obtain Man-N-HACC (Figure 2B). Infrared spectroscopy (FTIR) and nuclear magnetic resonance (NMR) ^{1}H spectroscopy was used to detect Man-N-HACC.

Preparation and Characterization of Man-N-HACC NPs/H1N1

Using the TPP crosslinking method, the preparation of Man-N-HACC NPs/H1N1 can be summarized as follows: Firstly, 200.00 mg of Man-N-HACC is dissolved in 10.0 mL of deionized water. Separately, 50.00 mg of TPP is dissolved in 10.0 mL of deionized water to prepare a TPP solution. Based on a mass ratio of 4:1 (Man-N-HACC: TPP), the TPP solution is slowly added to the Man-N-HACC solution at an appropriate stirring speed. The mixture is stirred for 15 minutes to obtain the Man-N-HACC NPs solution. Subsequently, the H1N1 influenza antigen is added to the above-mentioned nanoparticle solution in an incubator. The mixture is vortexed for 30 seconds and then stirred for 2 hours to obtain the Man-N-HACC NPs/H1N1.

To observe the morphology of the Man-N-HACC NPs, an appropriate amount of the sample is diluted with saline. The diluted sample is then negatively stained with phosphotungstic acid. After staining, the sample is dropped onto a copper grid specifically designed for electron microscopy and allowed to air-dry naturally. The morphology of the NPs is then observed using a transmission electron microscope. The particle size and distribution of the prepared samples are measured using a Malvern ZS 90 laser particle size analyzer.

Lectin Binding Test

Concanavalin A (Con A) lectin binding assay was used to confirm the successful affixation of mannose to the nanoparticle surface. Con A is a plant lectin that has been widely used as a model for studying protein-carbohydrate interactions.[16] Briefly, a 1 mg/mL solution of Man-N-HACC NPs was added to a 0.7 mg/mL solution of Con A in PBS and incubated with stirring at 37 °C for 1 hour. CS NPs were used as a negative control. After centrifugation at 10,000 rpm for 30 minutes at 4 °C, the samples were washed twice with PBS, and the particle size and polydispersity index (PDI) of the aggregates were measured using a Malvern particle size analyzer. Simultaneously, the turbidity changes of the mixed solution were monitored at 550 nm.

Preparation and Characterization of Man-N-HACC NPs/H1N1-Loaded dMAs

Man-N-HACC NPs/H1N1 were incorporated into a matrix solution to prepare Man-N-HACC NPs/H1N1 dMAs through a centrifugation-based molding method. Specifically, Man-N-HACC NPs /H1N1 were mixed with 30 wt% PVP K90 in a mass ratio of 1:12.5. To remove bubbles, the blended matrix solution was placed in a vacuum drying oven at a vacuum level of −80 KPa for 1 hour, resulting in a matrix solution containing Man-N-HACC NPs/H1N1. This solution was then used as the material for the microneedle body, while a blank 30 wt% PVP K90 matrix solution served as the backing material for the microneedles.

Using a proportion of 0.05 g/piece of the matrix solution for the front segment of the microneedles, centrifugation was performed at 4000 rpm for 5 minutes at 4 °C to fill the mold. Excess matrix solution was scraped off using a surgical scalpel. For the backing layer, a proportion of 0.15 g/piece of the backing matrix solution was used, and centrifugation was carried out at 4000 rpm at 4 °C. The microneedles were then dried and solidified at a constant temperature and humidity of 4 °C in a drug stability test chamber for 7 days, resulting in the formation of Man-N-HACC NPs/H1N1-loaded dMAs.

To observe the morphology of the Man-N-HACC NPs/H1N1-loaded dMAs, the microneedle bodies were placed under a high-magnification microscope for initial observation of the integrity of the microneedle shape and the condition of the tips. A scanning electron microscopy (SEM) was used to observe the surface morphology of the dMAs. Initially, the dMAs were placed on a sample stage coated with conductive adhesive and sputter-coated with gold in a small ion sputter coater. The gold-coated microneedles were then placed in a preheated SEM, and after the instrument stabilized, the SEM observation parameters (15.00 kV) were set to observe the morphology of the MNs.

Stability of Man-N-HACC NPs Alone and Within dMAs

Dynamic Light Scattering (DLS) technology was employed to measure changes in the particle size, polydispersity index (PDI), and Zeta potential of the NPs. This was used to assess the stability of Man-N-HACC NPs alone or in microneedle matrices. Specifically, Man-N-HACC NPs-loaded dMAs or Man-N-HACC NPs were stored at 4 °C, and samples were taken on days 1, 3, 7, 14 and 28 (only for Man-N-HACC NPs) for testing. The collected NPs were washed three times with deionized water to remove PVP as much as possible. A Malvern particle size analyzer was then used to measure the particle size, PDI, and Zeta potential at each time point. The final dMAs products were stored under vacuum at 4°C.

Mechanical Properties of Man-N-HACC NPs/H1N1-Loaded dMAs

To investigate the influence of NPs loaded into MNs on the mechanical properties of the dMAs, a universal testing machine was employed to investigate the minimum skin insertion force, compression behavior, and mechanical stress. Specifically, the universal testing machine was set to compression mode with a test rate of 0.02 mm/s and a trigger force of 0.01 N. A single metal microneedle with a length of 800 μm was adhered to the probe using double-sided tape. The displacement and the applied pressure exerted by the microneedle were recorded during the test, and the force at the point of abrupt change in the curve was identified as the minimum skin insertion force.

Maintaining the same skin insertion force conditions as described above, the dMAs are inverted and placed on the pressure plate with the needle tips facing upward, ensuring they were perpendicular to the plane of the probe for measurement. The test is completed when the displacement reached 500μm. At the end of the measurement, the dMAs were placed under a high-magnification microscope to observe whether the main body of the MNs and the tip of the needle were damaged to determine the mechanical stress of the dMAs.

Evaluation of Skin Penetration and Release Behavior of Man-N-HACC NPs/H1N1-Loaded dMAs

To confirm the insertion of microneedles, we employed excised porcine skin and optical coherence tomography (OCT) for scanning and observation. The MN array must be sufficiently sharp and robust to penetrate the stratum corneum of the skin, as discussed in our previous review.[17] To assess the penetration efficiency (PE) of the Man-N-HACC NPs/H1N1-loaded dMAs, we conducted a paraffin film puncture test and a skin puncture test on rats. The PE was calculated using the formula provided:

$$PE = \sum\left(\frac{D \times a}{A} \times L^{-1}\right) \tag{3}$$

a: the number of pores. A: total number of microneedles in a single patch. D: thickness of the paraffin film. L: height of the microneedle.

Specifically, the hair on the backs of rats was removed using hair removal cream and pet clippers. The dMAs were then mounted on a custom-made applicator for administration. After insertion, the applicator was maintained in a pressed position for 30 seconds before withdrawal. Immediately after removal, 0.5 mg/mL of methylene blue dye was applied to the treated area. After 30 seconds, excess dye was gently removed with absorbent cotton, and the punctured area was wiped with isopropyl alcohol to remove residual dye from the skin. Photographs of the treated rat skin were taken. After 2 hours, 4 hours, 8 hours, and 12 hours, the skin was wiped again with isopropyl alcohol, and additional photographs were taken to assess skin pore healing.

To evaluate the release behavior of dMAs, Rhodamine B was loaded into the dMAs and then inserted into a simulated model skin.[18] The dissolution of the dMAs was observed under a 3D microscope. With the help of Rhodamine B as a model drug, it can be visually identified by its prominent color.

Macrophage Internalization Assay of Man-N-HACC NPs

Internalization of Man-N-HACC NPs by immune cells was verified using the rat alveolar macrophage NR8383 cell assay. Briefly, NR8383 cells were seeded in a 6-well plate at a density of 5×10^5 cells/mL and incubated for 12 hours at 37 °C. Subsequently, 1.5 mL of FITC-labeled Man-N-HACC NPs and CS NPs were added to each well, followed by incubation for 2 hours. After incubation, the cells were centrifuged and washed three times with PBS. Flow cytometry analysis was then performed, and data acquisition and analysis were conducted using FlowJo 10.8.1 software.

Single Radial Immunodiffusion Assay (SRID)

SRID was used to quantify the amount of influenza HA antigen in a single patch of Man-N-HACC NPs/H1N1 dMAs.[19] Initially, agarose gel solution mixed with serum was poured onto a flat glass plate and accelerated to solidify at a low temperature of 2 °C. Holes were then punched into the gel plate to facilitate sample application. Standard antigens, along with a mixture solution of dissolved Man-N-HACC NPs/H1N1 dMAs and lysate (in a ratio of 9:1), were added to the respective holes. The gel plate was incubated overnight at 25 °C to allow for diffusion. Subsequently, the gel was stained with a 2% Coomassie Blue staining solution for 3 to 5 minutes. Following staining, the gel was then decolorized using a pre-prepared Coomassie Blue decolorization solution to enhance the visibility of the precipitation rings. Finally, the transverse and longitudinal diameters of the precipitation rings were measured using Image. J software, enabling the calculation of the HA antigen content in the Man-N-HACC NPs/H1N1-loaded dMAs.

Vaccination

To evaluate the immune response, Wistar rats aged 7~8 weeks were used for vaccination. All animal feeding and handling protocols in this study were approved by the Experimental Animal Ethics Committee of Zhejiang University of Technology and conducted in accordance with the "Guidelines for the Breeding and Use of Laboratory Animals" at Zhejiang University of Technology. Wistar rats were randomly divided into seven groups (n = 10): group 1, blank dMAs containing PBS; group 2, dMAs loaded with H1N1 antigen only; group 3, H1N1/poly (I:C) dMAs; group 4, Man-N-HACC/H1N1 dMAs; group 5, Man-N-HACC NPs/H1N1-loaded dMAs; group 6, 5% CS NPs/H1N1 dMAs; group 7, intramuscular injection (i.m). of H1N1 (without adjuvant). All groups received a dose of 3 μg of H1N1 antigen. A booster immunization was administered on day 14. Blood samples were collected on day 28, centrifuged at 10,000 rpm for 5 minutes to separate the serum, and stored at −20 °C until further use.

Hemagglutination Inhibition (HAI) Assay

The HAI titer is generally considered to be positively correlated with the protective efficacy of influenza vaccines.[20] Therefore, the immunogenicity of the Man-N-HACC NPs/H1N1-loaded dMAs is determined by measuring the HAI titer. To eliminate the influence of non-specific inhibitors, the rat serum samples require pretreatment with receptor-destroying enzyme. Briefly, the serum samples are treated with the receptor-destroying enzyme in a 37 °C water bath for 16–18 hours. Subsequently, a certain volume of chicken red blood cells (CRBCs) is added and incubated at 4 °C overnight. The pretreated serum samples are then serially diluted in a 96-well plate. An equal volume of inactivated H1N1 influenza virus stock (4 hA units) is added to each well, and the mixture is incubated at 25 °C for 30 minutes. Afterward, 25 μL of 1% CRBCs is added to each well, and the plate is shaken gently to mix the contents. The plate is then left undisturbed at room temperature for 30–45 minutes. The highest dilution of the serum that completely inhibits the agglutination of the CRBCs is considered as the HAI titer.

Enzyme-Linked Immunosorbent Assay (ELISA)

The total IgG antibody levels in the serum were determined by ELISA. Initially, the vaccine stock solution was diluted in coating buffer to a concentration of 3 μg/mL and used to coat the ELISA plates at 100 μL per well, incubating overnight at 4 °C. The plates were then washed six times with 350 μL of PBST (PBS solution containing 0.05% Tween 20) and blocked with 200 μL of blocking solution (5% w/v BSA in PBS) at 37 °C for 2 hours, followed by six washes with PBST.

The collected sera were diluted in a serial manner (10^n, where n = 1~6, ie, 10^1, 10^2, 10^3, 10^4, 10^5, 10^6). The negative control and PBS groups were not diluted. Each well received 100 μL of the diluted sera and was incubated at 37 °C for 1 hour, followed by six washes with PBST. Subsequently, 100 μL of goat anti-rat IgG antibody conjugated with HRP, diluted 1:5000, was added to each well and incubated at 37 °C for 1 hour. The plates were washed six times with PBST.

A 100 μL aliquot of 3.3′,5,5′-tetramethylbenzidine (TMB) substrate solution was added to each well for color development. The plates were incubated in the dark at room temperature for 25~30 minutes. Once a deep blue color appeared in the positive wells, the reaction was stopped by adding 50 μL of 1 M sulfuric acid. The optical density (OD) was measured at 450 nm using an ELISA reader, and the readings were recorded.

Data Analysis

All values reported in this study are presented as mean ± standard deviation (SD). Intergroup differences were analyzed using the *T*-test and Origin 2023b software, along with Prim software (V9, GraphPad). Significant differences were considered when $P < 0.05$ ($^*p < 0.05$, $^{**}p < 0.01$, $^{***}p < 0.001$, $^{****}p < 0.0001$).

Results

FTIR Characterization of N-HACC and Man-N-HACC

In the FTIR spectrum of CS (Figure 2C), a broad peak appears in the range of 3000~3600 cm^{-1} due to the presence of numerous O-H groups in CS that can form intermolecular hydrogen bonds. This association of O-H groups accounts for the broad peak observed in this range. Additionally, the N-H stretching vibration peak of CS is observed near 3416 cm^{-1}. The in-plane bending vibration peak of the primary amine N-H in CS appears at 1639 cm^{-1}. The absorption peak at 895 cm^{-1} is attributed to the symmetric stretching vibration of the β-glycosidic bond C-O in the CS ring. The C-N stretching vibration absorption peak in CS is present at 1384 cm^{-1}.

In the FTIR spectrum of N-HACC, the characteristic peaks of N-H and O-H are also observed in the range of 3000~3600 cm^{-1}. Comparative analysis with the FTIR spectrum of CS reveals sharp peaks in N-HACC at 3019 cm^{-1} and 1482 cm^{-1}, corresponding to the C-H stretching and bending vibration absorption peaks of the quaternary ammonium groups in N-HACC. Furthermore, the peaks for primary and secondary alcohols in the range of 1152~1072 cm^{-1} remain unchanged in N-HACC, indicating the successful introduction of the quaternary ammonium group at the -NH_2 site.

In contrast to N-HACC, significant changes are observed in the FTIR spectrum of Man-N-HACC. In the FTIR spectrum of Man-N-HACC, absorption peaks at 1617 cm^{-1} and 1412 cm^{-1} indicate the formation of Schiff bases (R-CH=N-R), confirming the successful synthesis of Man-N-HACC. The absorption peaks for C-H stretching and bending vibrations of the quaternary ammonium group are retained, and a slightly sharper peak is observed at 3410 cm^{-1}, which corresponds to the stretching vibration absorption peak of free hydroxyl groups. This suggests the successful introduction of mannose molecules. Additionally, the sharper peak at 3410 cm^{-1} indicates a lower degree of association of hydroxyl groups in N-HACC compared to Man-N-HACC.

^{1}H NMR Characterization of N-HACC and Man-N-HACC

^{1}H NMR spectroscopy was employed to confirm the structures of N-HACC and Man-N-HACC. As shown in Figure 2D, the proton signal at $\delta = 3.15$ ppm corresponds to the quaternary ammonium group (e) in N-HACC. The signal peak at $\delta = 4.46$ ppm represents the hydrogen at position 1 of N-HACC(d). By integrating the areas of these two peaks and using equ.(1), the quaternization degree (DQ) of N-HACC was calculated to be 75.26%. The assignments of the remaining peaks are indicated in Figure 2D.

Analysis of Figure 2E reveals that the signal peak at $\delta = 4.86$ ppm corresponds to the hydrogen at position 1 of the sugar ring in Man-N-HACC. The peak at $\delta = 2.45$ ppm represents the hydrogen at position 2 of the Man-N-HACC sugar ring. The proton signal at $\delta = 3.26$ ppm belongs to the quaternary ammonium group (Figure 2B) in Man-N-HACC. The multiplet peaks within the range of $\delta = 3.20$–3.81 ppm correspond to overlapping proton signals from chitosan and mannose, representing the protons of the chitosan backbone (C-3, C-4, C-5, C-6) and the mannose backbone. The proton signal at $\delta = 1.94$ ppm is attributed to the -N=CH-Man moiety(f) (Figure 2E) introduced after the mannose modification.

The obtained products were weighed, revealing that N-HACC was a white flocculent solid with a yield of 70.19%. The quaternization degree of N-HACC was calculated to be 75.26% using equ. (1). The resulting Man-N-HACC was a white solid with a yield of 62.81%. The degree of substitution of D-mannose was determined using elemental analysis (Table 1). By using Formula (2) to calculate the data in Table 1, we found that the degree of substitution of D-mannose of Man-N-HACC was 12.65%.

Physicochemical Properties of Man-N-HACC NPs

The effects of different mass ratios of Man-N-HACC and TPP on the formation of NPs were studied. Experimental results indicate that Man-N-HACC NPs exhibit optimal physicochemical properties when the mass ratio of Man-N-HACC to TPP reaches 4:1. As the mass ratio increases, both the size and PDI of Man-N-HACC NPs show an

Table 1 Elemental Analysis Data of N-HACC and Man-N-HACC

	C (%)	N (%)	H (%)	Ratio of C/N
N-HACC	37.05	7.06	8.54	5.25
Man-N-HACC	40.62	6.45	7.30	6.30

Abbreviations: C, Carbon; N, Nitrogen; H, Hydrogen.

https://doi.org/10.2147/IJN.S502724

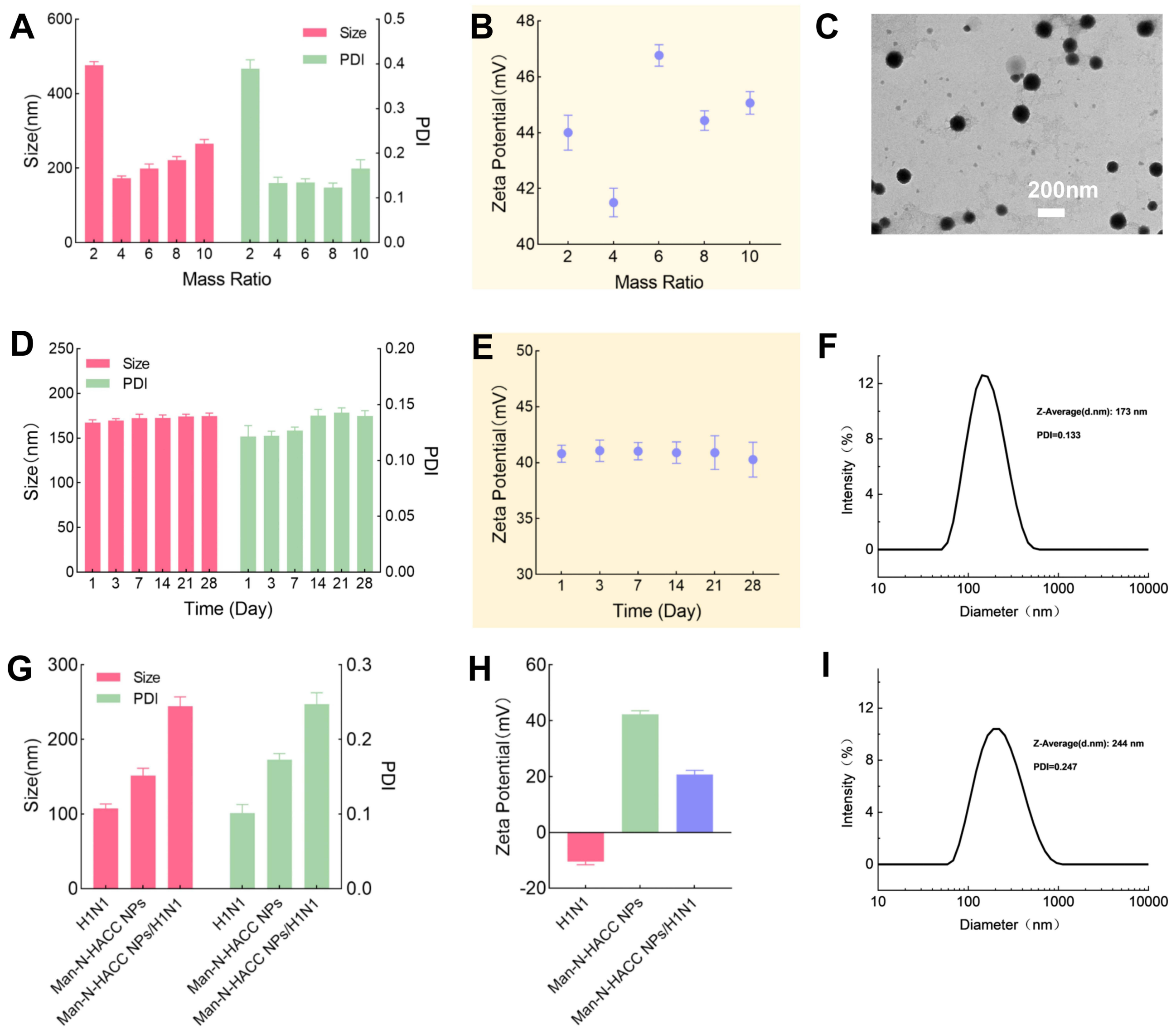

Figure 3 Physicochemical properties of the prepared Nps. (**A**) Impact of TPP concentration on the particle size and PDI of NPs. (**B**) Effect of TPP concentration on the Zeta potential of NPs. (**C**) TEM image of Man-N-HACC NPs, scale bar: 200 nm. (**D**) Particle size distribution of Man-N-HACC NPs. (**E**) Changes in particle size and PDI of Man-N-HACC NPs over 28 days at 4 °C. (**F**) Changes in Zeta potential of Man-N-HACC NPs over 28 days at 4 °C. (**G**) The size and PDI of H1N1, Man-N-HACC NPs and Man-N-HACC NPs/H1N1. (**H**) The Zeta potential of H1N1, Man-N-HACC NPs and Man-N-HACC NPs/H1N1. (**I**) Particle size distribution of Man-N-HACC NPs/H1N1.

increasing trend (Figure 3A and B). Therefore, to obtain ideal Man-N-HACC NPs, we chose to crosslink Man-N-HACC with TPP at a mass ratio of 4:1.

Transmission electron microscopy (TEM) observation shows that the NPs exhibit a nearly spherical morphology with a diameter less than 200 nm (Figure 3C), which is consistent with the results of dynamic light scattering measurement in Figure 3D, with an average size of 173 nm. Furthermore, stability study showed that the size, PDI and Zeta potential of Man-N-HACC NPs remained almost constant over 28 days (Figure 3E and F). Man-N-HACC NPs/H1N1 were prepared by dripping negatively charged H1N1 antigens into the Man-N-HACC NPs solution. Figure 3B reveals that Man-N-HACC NPs have a high Zeta potential of 40.5 mV, which is beneficial for negative antigen binding; the H1N1 antigen particles have an average size of 108 nm and a Zeta potential of −10.24 mV (Figure 3G and H), indicating their negative charge properties. When H1N1 antigens bind to Man-N-HACC NPs to form Man-N-HACC NPs/H1N1, the Zeta potential decreases to 20.74 mV (Figure 3H), and average size increases to 244 nm (Figure 3G and I). This decrease in Zeta potential further demonstrates that H1N1 antigen particles are adsorbed onto the surface of Man-N-HACC NPs, effectively shielding the strong positive charge of Man-N-HACC NPs. This result not only validates the crucial role of electrostatic interactions in the binding process between Man-N-HACC NPs and H1N1 antigens but also provides an important physicochemical basis for subsequent biomedical applications.

Stability of Man-N-HACC NPs in dMAs

According to the measurements by Malvern ZS 90, the particle size (Figure 4A) and PDI (Figure 4B) of NPs within dMAs gradually increased over time. This observation could be attributed to partial adhesion of NPs caused by the microneedle matrix, leading to aggregation phenomena. However, there were no significant differences between the results, indicating that the NPs within dMAs exhibited good colloidal stability under storage conditions. Compared to free NPs, those within dMAs exhibited larger particle sizes and PDI values at 4 °C. Conversely, the Zeta potential of NPs within dMAs was lower, further suggesting that the presence of the microneedle matrix shielded the strong positive charge on the surface of the NPs.

This phenomenon of NPs stability within dMAs is crucial for their effective delivery and performance. The colloidal stability ensures that the NPs remain intact and do not degrade during storage, while the lower Zeta potential may facilitate better compatibility with the microneedle matrix and enhance their retention within the needles. Overall, these results indicate that Man-N-HACC NPs can maintain their structural integrity and physicochemical properties within the microneedle delivery system, making them suitable for transdermal applications.

Spatial Orientation of Mannose Ligands

Concanavalin A (Con A) possesses four binding sites that can interact with mannose. Due to the strong interaction between Con A and mannose, Con A serves as a crosslinking agent, enabling the formation of cross-linked complexes between the two components, leading to precipitation from the solution.[21] Therefore, the binding behavior between Man-N-HACC NPs and Con A was investigated using UV-visible spectrophotometry.

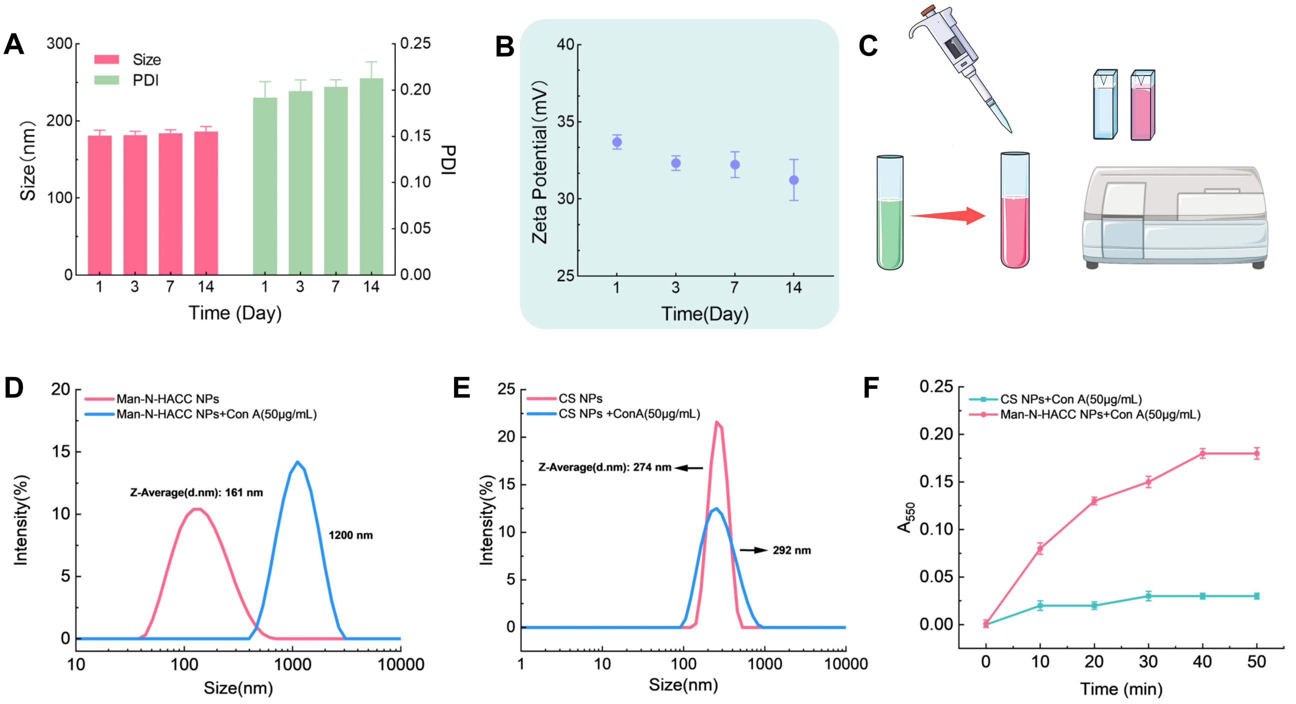

Figure 4 Stability of Man-N-HACC NPs in MNs and characteristic changes upon binding with Con A (50 μg/mL). (**A**) Changes in particle size and PDI of Man-N-HACC NPs within MNs over 14 days at 4 °C. (**B**) Changes in Zeta potential of Man-N-HACC NPs within MNs over 14 days at 4 °C. (**C**) Schematic diagram of the lectin binding test. (**D**) Changes in particle size of Man-N-HACC NPs before and after binding with Con A (50 μg/mL). (**E**) Changes in particle size of CS NPs before and after binding with Con A (50 μg/mL). (**F**) Turbidity changes at 550 nm for Man-N-HACC NPs and CS NPs incubated with Con A (50 μg/mL).

https://doi.org/10.2147/IJN.S502724

After incubation with Con A solution for 1 hour, the size of Man-N-HACC NPs increased from 161 nm to 1200 nm, indicating that Con A triggered the aggregation of Man-N-HACC NPs (Figure 4C and D). In contrast, no aggregation was observed for CS NPs (Figure 4E). Additionally, upon the application of the same concentration of Con A solution, the absorbance of Man-N-HACC NPs increased in a time-dependent manner, whereas no increase in absorbance was observed for CS NPs. After 40 minutes, no significant changes in absorption values were observed, suggesting that the binding sites on the surface of Man-N-HACC NPs gradually reached saturation (Figure 4F).

These two experiments demonstrate that the surface of Man-N-HACC NPs contains a certain number of mannose molecules that can specifically bind to MR. This spatial orientation of mannose ligands on the NPs surface is crucial for their targeting capabilities, enabling them to effectively interact with cells expressing mannose receptors, such as macrophages and dendritic cells, for potential applications in immunotherapy and vaccine delivery.

Microstructural Characterization and Mechanical Properties of Man-N-HACC NPs/H1N1-Loaded dMAs

Figure 5 shows the structural properties of dMAs as observed with high-resolution electron microscopy and focused ion beam techniques. SEM images revealed differences in the microstructures of microneedles in which NPs were unloaded (Figure 5A–C) or loaded with different amounts (Figure 5D–I). The NPs were primarily concentrated at the tips of the dMAs and were compactly encapsulated, forming a “concrete-like model”. (Figure 5D–I). This configuration ensures the complete delivery of the antigen into the skin, minimizing vaccine waste and increasing the effective delivered dose. The surface of 1% NPs dMAs exhibited a smoother texture, while 5% and 10% NPs dMAs exhibited a porous and rough texture, resembling a “sand-concrete” state. These morphologies reflected the disperse distribution of Man-N-HACC NPs at the tips of the dMAs. The internal structure of the dMAs tips were fractured and visualized using SEM. The results showed that the Man-N-HACC NPs within the MNs tips were spherical and had sizes similar to those measured using TEM, indicating no significant aggregation.

The mechanical properties of dMAs with different concentrations of Man-N-HACC NPs were characterized using a 3D microscope (Figure 5D) and a universal testing machine. The displacement-force curve of a single 800 μm metal microneedle pressing against porcine skin is shown in Figure 5E. At a displacement of 0.18 mm, the force decreased sharply at 0.069 N, indicating that the microneedle punctured the skin. The insertion force of this needle type was determined to be 0.069 N (Figure 5J). The 1% Man-N-HACC NPs/H1N1 dMAs could withstand a mechanical stress of 11.77 N under a compressive force of 500 μm, while the 5% and 10% NPs dMAs could withstand 9.73 N and 6.90 N, respectively (Figure 5K). Notably, the mechanical properties of the 5% Man-N-HACC NPs/H1N1 dMAs were superior to the other two groups, suggesting that the appropriate addition of NPs enhances the mechanical performance of the microneedles. Similarly, a full view of the NPs dMAs was observed with the 3D microscope, and all the appearance specifications were in accordance with the design requirements (Figure 5L and 5M).

These results provide valuable insights into the structural integrity and mechanical robustness of the dMAs, which are crucial for their effective delivery and safety in transdermal applications. The optimal concentration of NPs within the dMAs was identified, balancing the need for antigen delivery with the mechanical requirements for successful skin penetration.

Skin Penetration and Release Behavior of Man-N-HACC NPs/H1N1-Loaded dMAs

To better observe the ability of microneedles with different concentrations of Man-N-HACC NPs to penetrate the skin, as well as to determine the penetration rate of the Man-N-HACC NPs/H1N1-loaded dMAs, we employed optical coherence tomography (OCT) to scan and image the penetration sites. The images obtained reveal that both the 1% and 5% NPs microneedles effectively pierce the stratum corneum of the skin, without bending or breaking upon contact with the skin (Figure 6A and B). Analysis using Image J software indicates a penetration depth of up to 500 μm. However, the 10% NPs microneedles did not fully penetrate the stratum corneum of porcine skin (Figure 6C).

Using a paraffin film puncture test (Figure 6D), the penetration efficiency of 5% the Man-N-HACC NPs/H1N1-loaded dMAs was calculated to be 90% according to equ. (3). To characterize the dissolution behavior of Man-N-HACC

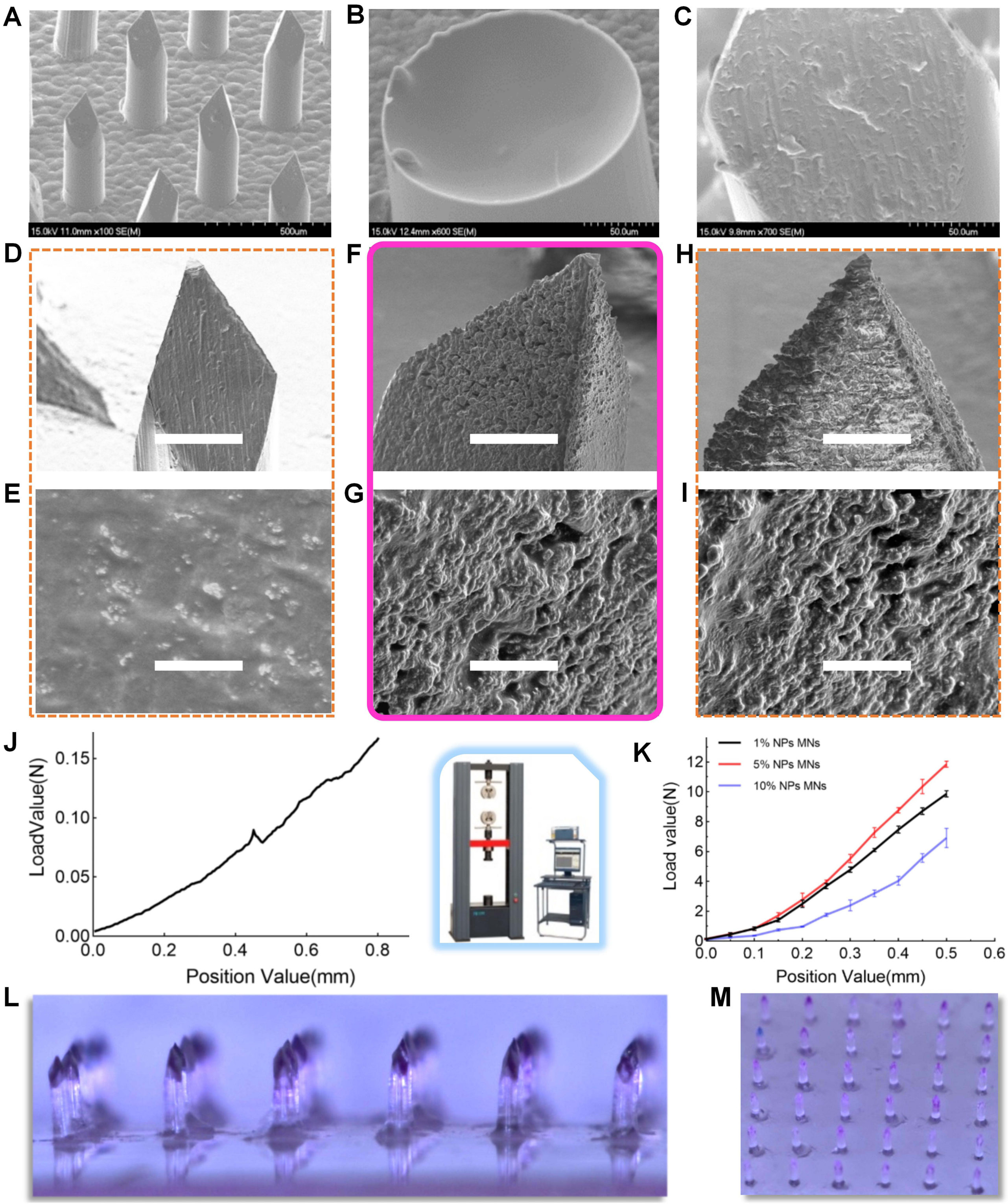

Figure 5 SEM Imaging and mechanical characterization of NPs dMAs. SEM images of arrays (**A**), cross section (**B**) and tip local (**C**) without NPs-loaded dMAs. SEM images of 1% NPs-loaded dMAs array s tip local (**D**, scale bar: 50 μm) and amplified (**E**, scale bar: 5 μm). SEM images of 5% NPs-loaded dMAs tip local (**F**, scale bar: 50 μm) and amplified (**G**, scale bar: 5 μm). SEM images of 10% NPs-loaded dMAs tip local (**H**, scale bar: 50 μm) and amplified (**I**, scale bar: 5 μm). Insertion force of single microneedles loaded with 5% NPs (**J**) and mechanical properties of dMAs loaded with 1–10% NPs (**K**) tested by a high-sensitivity universal testing machine. Side (**L**) and top (**M**) views of NPs dMAs.

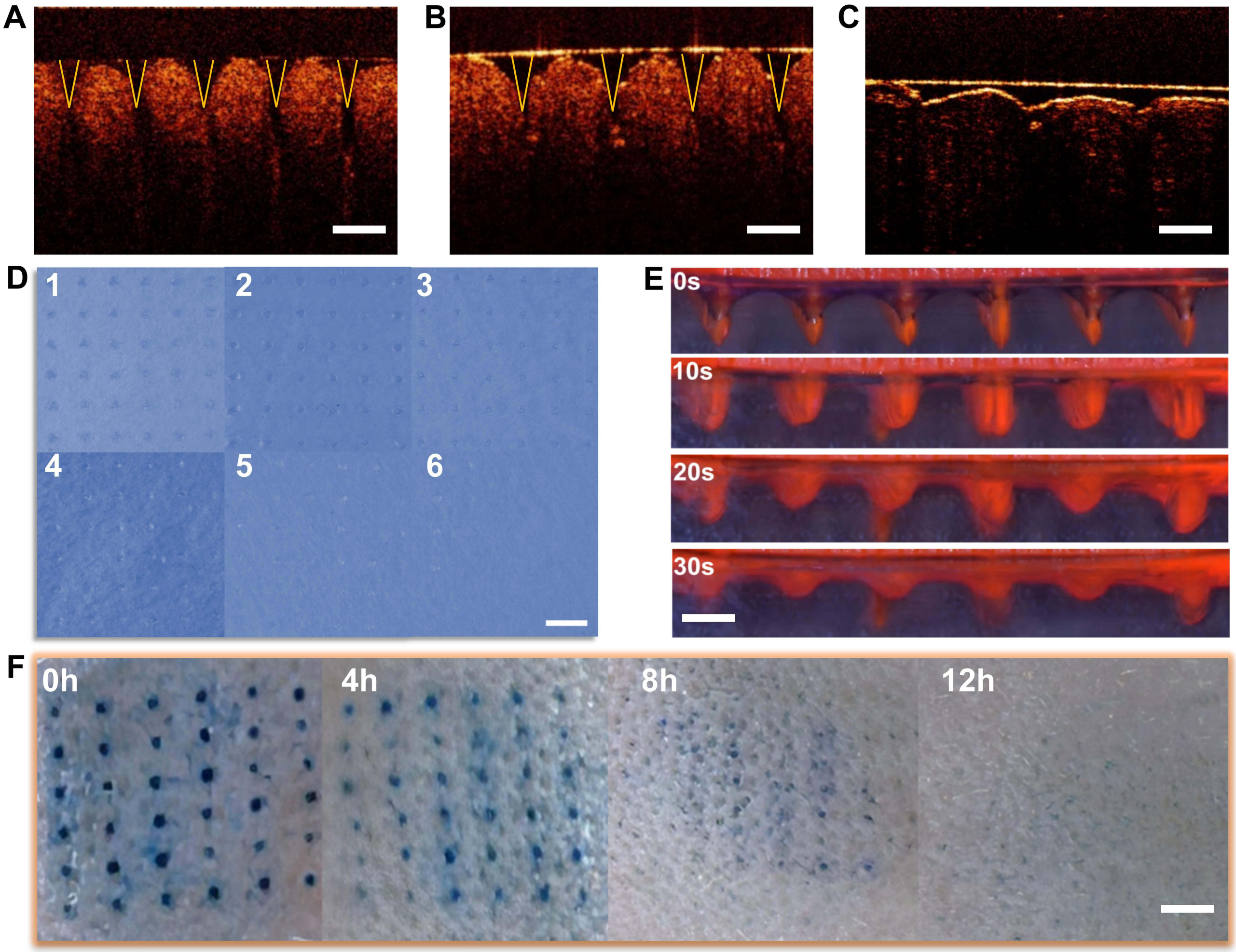

Figure 6 Performance of NPs dMAs penetrating simulated and real skins. (**A**) OCT image of 1% NPs dMAs penetrating the skin, scale bar: 600 μm. (**B**) OCT image of 5% NPs dMAs penetrating the skin, scale bar: 600 μm. (**C**) OCT image of 10% NPs dMAs s penetrating the skin, scale bar: 600 μm. (**D**) Results of the paraffin film puncture test for 5% NPs dMAs, scale bar: 1000 μm, 1–6 layer from top to bottom. (**E**) Illustration of the microneedle penetrating model skin with Rhodamine B as a model drug, scale bar: 600 μm. (**F**) Healing of skin pores within 12 hours, scale bar: 800 μm.

NPs/H1N1-loaded dMAs in the skin, rhodamine B was used as a model drug. Figure 6E shows that the microneedles were basically dissolved and rhodamine B was released within 30s, which demonstrated that NPs could diffuse rapidly after the dMAs were punctured into the skin. When the dMAs patch was applied to the back skin of a rat using a patch applicator and then stained with methylene blue for 2 minutes, it was observed that all the microneedles successfully pierced the skin (Figure 6F). After 12 hours, the pores formed by the microneedles had closed (Figure 6F), indicating that the wounds healed within a relatively short period, thus minimizing the risk of infection.

The results obtained from these experiments demonstrate the feasibility and efficiency of Man-N-HACC NPs dMAs in penetrating the skin barrier and releasing their payload. The optimal concentration of NPs within the dMAs was found to be crucial for successful skin penetration, while also ensuring rapid wound healing and minimal discomfort for the individual.

Macrophage Internalization Assay Results

Rat alveolar macrophage NR8383 cells with a high density of mannose receptors on the surface were subjected to cell internalization experiments to further validate the immune cell targeting effect of mannose-modified NPs. Flow cytometry was employed for quantitative assessment of NP internalization. Figure 7A shows that the internalization rates of macrophages for CS NPs and Man-N-HACC NPs were 21% and 45%, respectively. These findings indicate that

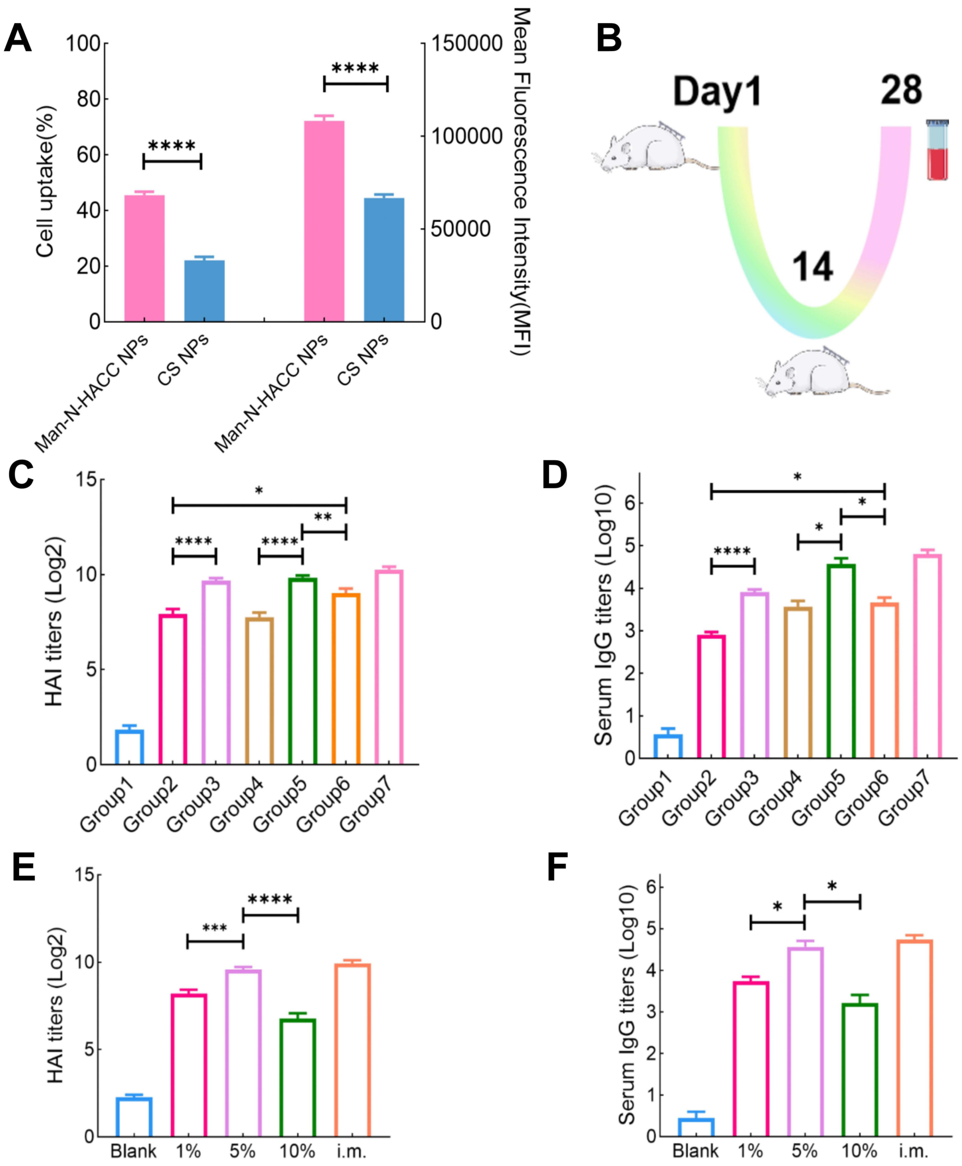

Figure 7 Immunization schedule and results of HAI and IgG antibody titer determination. (**A**) Quantitative analysis of cell internalization and intracellular fluorescence intensity for two different NPs. ****$p < 0.0001$. (**B**) Schematic representation of the immunization protocol. (**C**) HAI titers of different groups: group 1 (Blank dMAs containing PBS), group 2 (dMAs loaded with H1N1 antigen only), group 3 (H1N1/poly (I:C) dMAs), group 4 (Man-N-HACC/H1N1 dMAs), group 5 (5% Man-N-HACC NPs/H1N1 dMAs), group 6 (5% CS NPs/H1N1 dMAs), and group 7 (i.m. of H1N1). (**D**) IgG antibody titers of different groups. (**E**) HAI titers of microneedle patches with varying NPs concentrations: Blank (Blank dMAs containing PBS), 1% (1% Man-N-HACC NPs/H1N1 dMAs), 5% (5% Man-N-HACC NPs/H1N1 dMAs), and 10% (10% Man-N-HACC NPs/H1N1 dMAs). (**F**) IgG antibody titers of dMAs with varying NPs concentrations. *$p < 0.05$, **$p < 0.01$, ***$p < 0.001$, ****$p < 0.0001$.

the mannose modification enhances the efficiency of immune cell internalization of NPs, as corroborated by the mean fluorescence intensity. Man-N-HACC NPs can effectively target dendritic cells and macrophages through the mannose receptors exposed on the surface of immune cells, crucial for antigen presentation and internalization.

The targeted delivery of drugs or vaccines via Man-N-HACC NPs to these immune cells holds promise for improving the immunogenicity and therapeutic efficacy of various immunological interventions. The ability to specifically target and enhance the internalization by immune cells represents a significant step towards more efficient and tailored immune therapies.

Immunological Evaluation

HAI titer is positively correlated with the strength of the immune response. Serum samples collected from rats immunized twice with different formulations were assayed through hemagglutination inhibition tests and ELISA to evaluate the intensity of immune responses induced by various vaccine formulations. The results of immunoassay on the 28th day of the terminal (Figure 7B) are shown in Figure 7C–F.

In Figure 7C, the Man-N-HACC NPs/H1N1-loaded dMAs group (GMT = 891) exhibited comparable HAI titer levels to the H1N1 i.m. group (GMT = 1176). There was no statistically significant difference in the geometric mean titers (GMT) of HAI between the two groups ($p > 0.05$). Similarly, the IgG antibody titer levels in both groups showed a similar trend (Figure 7D), indicating that the Man-N-HACC NPs/H1N1-loaded dMAs can provide a comparable level of immune protection as intramuscular injection of the influenza vaccine. The HAI titer level induced by the Man-N-HACC NPs/H1N1-loaded dMAs group was twice that of the 5% CS NPs/H1N1 dMAs group (GMT = 445.7), primarily attributed to the immune targeting effect of the mannose ligands on the surface of Man-N-HACC NPs.

Surprisingly, the Man-N-HACC NPs/H1N1-loaded dMAs group elicited a significantly higher HAI titer level compared to the Man-N-HACC/H1N1 dMAs group (GMT = 194) ($p < 0.001$), highlighting the critical role of the nanoparticle structure. Moreover, the Man-N-HACC/H1N1 dMAs group only generated a slightly higher HAI titer level than the H1N1 dMAs group (GMT = 207.9), suggesting that the Man-N-HACC material exhibits a stronger immunogenic adjuvant effect when formulated into NPs. Similarly, the total IgG antibody titer levels in serum showed similar results to the HAI titer levels (Figure 7D). The virus-specific IgG antibody level in the Man-N-HACC NPs/H1N1-loaded dMAs group (GMT = 19953) was comparable to that in the H1N1 i.m. group (GMT = 31623) and was 7.9 times higher than that in the 5% CS NPs/H1N1 dMAs group (GMT = 2512). The IgG antibody levels in the Blank dMAs, H1N1 dMAs, and Man-N-HACC/H1N1 dMAs groups were 1.995, 631, and 1995, respectively, with no significant difference between the latter two groups.

Rats were immunized with dMAs containing different concentrations of NPs, and the serum HAI titers and total IgG antibody titers were measured to help us determine the optimal amount of Man-N-HACC NPs. The results are shown in Figure 7E and F. The 5% Man-N-HACC NPs/H1N1-loaded dMAs group exhibited the highest HAI titer (GMT = 724.1) and IgG antibody titer (GMT = 19953) levels. Notably, the 10% NPs dMAs group showed the lowest levels of HAI titer (GMT = 84.45) and IgG antibody titer (GMT = 631), possibly due to incomplete insertion of the dMAs caused by the excessive amount of NPs, resulting in reduced patch insertion efficiency. IgG antibody subtypes and other relevant immune response indicators will be of particular interest and deserve systematic investigation and analysis after the engineering exploration of this preparation technique is completed. In summary, our study provides a proof-of-concept demonstration, and these results confirm the advantages of Man-N-HACC NPs/H1N1 dMAs in the delivery of split influenza vaccines.

Discussion

NPs facilitate the internalization of vaccines through receptor-mediated endocytosis by APCs, thereby enhancing antigen presentation and triggering $CD4^+$ and $CD8^+$ T cell immune responses. This modulation of both humoral and cellular immunity is crucial for combating viral infections.[22,23] Split influenza vaccines, lacking pathogen-associated molecular patterns (PAMPs), are not easily recognized by APCs. Therefore, effective delivery systems and adjuvants that mimic PAMPs are necessary to improve the immune response against pathogens.[24] Nanoparticle vaccine delivery systems are pivotal in addressing these challenges, offering promising potential for the development and application of split influenza vaccine products. In particular, polysaccharide NPs, such as chitosan and its derivatives, and curdlan, can interact with antigen-presenting cells, increasing antigen uptake and presentation through receptor recognition, and triggering robust immune responses.[25,26] These adjuvants have been applied in various diseases, including hepatitis B, influenza, and COVID-19,[27] improving antibody titers and protection to a certain extent.

Typically, NPs can bind to antigens in four primary ways: surface chemical conjugation, encapsulation, electrostatic adsorption, and blending.[28] Surface chemical conjugation is a destructive strategy, as certain chemical conjugation agents may deactivate fragile antigens, making it difficult to induce an effective immune response.[29] Encapsulating antigens within NPs can protect them well, but may result in a slow release rate, potentially leading to immune tolerance issues. Utilizing the surface properties of NPs for electrostatic adsorption of antigens is a commonly applied method, as it avoids the drawbacks of the first two methods and is relatively gentle. In the overall nanoparticle vaccine delivery system, not all NPs can fully adsorb antigens; some NPs remain in a blended state with antigens. The high surface energy effect of

NPs[30] and the targeting effect of surface-specific ligands provide more opportunities for mannose ligands to bind to MRs on the surface of APCs, enhancing the passive targeted delivery of vaccine components to the immune response-generating centers of the lymph nodes (LNs), providing a lymphatic transport advantage.[31] The favorable lymph node drainage promoted by NPs may be a common characteristic of this formulation form.[32] In our previous research, it was hypothesized that during the endocytosis of NPs by APCs, antigens are taken up by APCs in a "hitchhiking" manner.[33]

The MR is a recycling receptor that endocytoses and internalizes ligands to early endosomes and then returns to the plasma membrane,[34] playing an important role in the recognition of PAMPs and the initiation of innate immunity. However, as a specific ligand for MR, mannose directly incorporated into the vaccine delivery system cannot serve as a guide for vaccine endocytosis and is usually chemically conjugated to the delivery medium or antigen. Chemical modification of antigens may disrupt their components and affect their activity. Therefore, we grafted mannose onto N-HACC molecules, which are positively charged and have been proven to have certain adjuvant effects,[35] forming Man-N-HACC to give it targeting properties. There have been reports on the preparation and application of this material prior to this study.[36] Our previous research also demonstrated that mannose-grafted PLGA-PEG NPs have excellent immune cell targeting capabilities.[33] These studies provide valuable information. We employed a completely different TPP cross-linking method from the literature[36] to prepare this material into NPs. This cross-linking technique ensures the display of mannose groups on the surface of the NPs, thereby guaranteeing their effectiveness in targeting APCs such as macrophages and dendritic cells. This was confirmed in the Con A binding experiment in this study, which demonstrated the exposure of mannose residues on the surface of Man-N-HACC NPs, and in the uptake test of these NPs by rat alveolar macrophages NR8383, which showed that the sensitivity of Man-N-HACC NPs to macrophage internalization was twice that of non-mannosylated CS NPs. This study indicates the importance of nanostructures in enhancing the immune effects of adjuvant materials and vaccines. Man-N-HACC NPs have a particle size of 100~200 nm, a Zeta potential of 40.5 ±3.2 mV, and are spherical with a rough surface. The Zeta potential is an important parameter reflecting the surface charge characteristics of particles, indicating the interactions (attraction and repulsion) between NPs.[37] The binding of NPs to antigens is achieved through electrostatic adsorption, aiming to minimize the impact of the loading process on antigen activity. Split influenza antigens bind to the surface of Man-N-HACC NPs, and compared to NPs with a negative surface charge, Man-N-HACC NPs with a strong positive charge exhibit higher antigen adsorption capacity, enabling effective absorption by APCs to enhance immune responses. At the same time, the binding of NPs to the vaccine results in their own slow diffusion and gradual release of H1N1 antigen, which is also beneficial for sustained immune stimulation. Our results suggest that Man-N-HACC NPs could serve as a safe alternative to poly(I: C) and may reduce the required antigen dose to achieve similar immune responses, although further validation is needed. Utilizing the adjuvant properties of mannose and the antigen-binding capabilities of N-HACC, our Man-N-HACC NPs offer a promising approach for the development of influenza vaccines.

Recent research has demonstrated that controlling the release of antigens from a NPs reservoir in the skin following transdermal vaccination through MNs is a powerful strategy to extend the exposure time of antigens and activate interactions between dendritic cells and antigen components.[38,39] MNs can precisely and multi-pointedly deliver vaccines into the skin, which is extremely challenging for other delivery technologies to realize. Therefore, the combination of NPs-loaded vaccines with dMAs represents an innovative platform for sustained antigen release and targeted transdermal vaccine delivery. This approach achieves immunogenicity on par with virus-derived methods and broadens the scope of protection. Moreover, compared to the direct delivery of soluble antigens through MNs, the addition of NPs helps enhance the mechanical strength of MNs, as verified in our previous research.[40] NPs are primarily concentrated at the tips of dMAs (Figure 5F) and are compactly encapsulated, forming a "concrete-like model" that strengthens the dMAs (Figure 5K). This ensures the complete delivery of antigens into the skin, reducing antigen loss. The study found that the 5% CS NPs/H1N1 dMAs group induced a certain level of humoral immunity, but it was difficult to achieve a high-level immune response in rats using H1N1 alone. Notably, we unexpectedly found that the 5% Man-N-HACC NPs/H1N1 dMAs group elicited higher HAI titers than the Man-N-HACC/H1N1 dMAs group, with a similar trend observed in serum IgG measurements. There may be several reasons for this: First, when Man-N-HACC material is encapsulated with antigen at the tip of a rapidly dissolving MNs, it may not act as an effective adjuvant due to the rapid release of antigen. In contrast, when Man-N-HACC NPs (as a potent adjuvant) are electrostatically bound to antigens and delivered to the dermis via MNs, they are slowly released at the injection site, continuously stimulating the immune system, causing recruitment of immune cells, producing a long-lasting cascade effect, and enhancing the immune response. Second, the spatial arrangement of mannose ligands affects the specificity of receptor binding, as evidenced by the studies of Haifei Gao.[41] The spatial arrangement of mannose molecules grafted onto Man-N-HACC is different from that on the surface of Man-N-HACC NPs, which may explain why the former is not effective in stimulating APCs. Mannose molecules on the surface of Man-N-HACC NPs may have a higher binding affinity for MR, a process that needs to be investigated in further detail.

It was observed that the immunological efficacy of the 5% Man-N-HACC NPs delivered via dMAs did not surpass that of the intramuscular injection of H1N1 vaccine. There are possibly two important reasons for this outcome. First, the MNs-based vaccine undergoes multiple processing steps, and despite our protective measures, some loss of vaccine activity is inevitable during these processes, resulting in the final dose used in animal experiments being lower than the intended dose, which was designed to be identical for both groups. Our previous repeated assessments using the SRID test to measure the potency of H1N1 in MNs patches indicated a 10–35% reduction in potency due to the preparation process. Given that the SRID method itself has an approximate 20% methodological error, accurately determining the actual potency of H1N1 in MNs patch becomes challenging. The performance of SRID is not satisfactory in some cases, especially in the detection of low concentration samples.[42] Developing more precise potency measurement methods will be essential to address this issue.[43] The second reason is that in this study, we adopted the widely-used twice-immunization schedule within 28 days in the influenza vaccine industry to evaluate vaccine immunogenicity. This approach did not allow us to observe potential differences in immune responses at other time points beyond day 28. Research on immune persistence and determination of the optimal endpoint for vaccination are indeed crucial for assessing vaccine efficacy. Comparative studies on MNs and NPs vaccine delivery systems with respect to immunization intervals and persistence of immunity are also in preparation. We hope to elaborate on these in a separate report.

By harnessing the unique properties of NPs and dMAs, we can develop more effective and innovative vaccine delivery systems that enhance immune responses and protect against influenza and other diseases. Furthermore, it is reasonable to believe that different combinations of NPs with MNs will have an impact on the final pharmacological or immune effect. Following this proof-of-concept study, more exploratory work on targeting materials and their NPs via various MNs types or other delivery modalities is in progress or will be scheduled. These studies include research on the interaction mechanisms between NPs and immune cells, investigations into different immunization periods and immune durability of vaccine delivery systems for MNs and NPs, and explorations at both the technical and immunological levels of MNs to truly achieve the multi-point immunization effect that MNs can provide, which is expected to be superior to that of a single-point injection. Multi-point administration has been shown to effectively enhance the immune response and increase antibody titers.[44,45] Although MNs patches are theoretically capable of providing superior immune stimulation due to multiple skin entry points, variables such as the administration site, vaccine potency, concentration, antigen morphology and diffusivity, immune response patterns, and the characteristics of the vaccinated individuals make the relationship between inter-point distance and immune response highly complex. However, this efficacy is contingent upon whether the distance between injection points can trigger multi-regional stimulation. Therefore, it is worth exploring to determine the appropriate injection point spacing for specific vaccines. To this point, no such research has been carried out within the context of microneedle arrays.

Conclusion

In this study, we have successfully synthesized Man-N-HACC NPs, which exhibit uniform sizes and rough spherical surfaces. These NPs demonstrate good colloidal stability over a period of four weeks. Lectin binding experiments conducted in vitro have confirmed the exposure of mannose on the surface of the NPs, imparting them with virus-like structures and components. Man-N-HACC NPs are efficiently absorbed by rat alveolar macrophages, exhibiting good targeting of immune cells. By loading Man-N-HACC NPs into the tips of rapidly dissolving MNs, we have created a “sand-concrete” model that effectively enhances their mechanical properties. Man-N-HACC NPs remain stable within the MNs, ensuring long-term stability of the antigen. The Man-N-HACC NPs/H1N1-loaded dMAs are capable of inducing sufficient systemic immunity and are particularly suitable for the delivery of vaccines lacking intact viral structures. The convenient delivery advantage of the MNs patch allows for self-administration of vaccines, thereby enhancing vaccination efficiency. In conclusion, this engineering proof-of-concept study confirms that a delivery system combining Man-N-HACC NPs with dMAs has proven to be an effective and safe platform for split influenza vaccine delivery.

Abbreviations

MNs, microneedles; NPs, nanoparticles; dMAs, dissolvable microneedle arrays; APCs, antigen presenting cells; TLRs, Toll-like receptors; CLRs, C-type lectin receptors; MRs, mannose receptors; CRDs, carbohydrate recognition domains; CS, chitosan; N-HACC, N-2-hydroxypropyl trimethyl ammonium chloride chitosan; TPP, Tripolyphosphate; FTIR, Fourier Transform Infrared Spectroscopy; NMR, Nuclear Magnetic Resonance; Con A, Concanavalin A; PDI, polydispersity index; DLS, dynamic Light Scattering; SEM, scanning electron microscopy; OCT, optical coherence tomography; TEM, Transmission electron microscopy; PE, penetration efficiency; SRID, single radial immunodiffusion assay; HAI, hemagglutination inhibition assay; CRBCs, chicken red blood cells; ELISA, Enzyme-Linked Immunosorbent Assay; PAMPs, pathogen-associated molecular patterns.

Data Sharing Statement

Data will be made available on request.

Acknowledgment

This work was funded by the Research Project of Zhejiang Chinese Medical University (2023JKJNTZ07), the Science and Technology Project of Traditional Chinese Medicine of Zhejiang Province (2025ZR114), the Research Fund for the Provincial Universities of Zhejiang (RF-C2022004), and the Key Science and Technology Innovation Team of Zhejiang Province [2013TD15].

Author Contributions

All authors made a significant contribution to the work reported, whether that is in the conception, study design, execution, acquisition of data, analysis and interpretation, or in all these areas; took part in drafting, revising or critically reviewing the article; gave final approval of the version to be published; have agreed on the journal to which the article has been submitted; and agree to be accountable for all aspects of the work.

Disclosure

The authors declare that they have no known competing financial interests or personal relationships that could have appeared to influence the work reported in this paper.

References

1. Uyeki TM, Hui DS, Zambon M, et al. Influenza. *Lancet*. 2022;400(10353):693–706. doi:10.1016/S0140-6736(22)00982-5
2. Nir Y, Paz A, Sabo E, et al. Fear of injections in young adults: prevalence and associations. *Am J Trop Med Hyg*. 2003;68(3):341–344. doi:10.4269/ajtmh.2003.68.341
3. Liu T, Luo G, Xing M. Biomedical applications of polymeric microneedles for transdermal therapeutic delivery and diagnosis: current status and future perspectives. *Adv Ther*. 2020;3(9). doi:10.1002/adtp.201900140
4. Zhang L, Xiu X, Li Z, et al. Coated porous microneedles for effective intradermal immunization with split influenza vaccine. *ACS Biomater Sci Eng*. 2023;9(12):6880–6890. doi:10.1021/acsbiomaterials.3c01212
5. Song JM, Kim YC, E O, et al. DNA vaccination in the skin using microneedles improves protection against influenza. *mol Ther*. 2012;20(7):1472–1480. doi:10.1038/mt.2012.69
6. Ellison TJ, Talbott GC, Henderson DR. Intradermal delivery of a quadrivalent cell-based seasonal influenza vaccine using an adjuvanted skin patch vaccination platform. *Vaccine*. 2023;41(2):304–314. doi:10.1016/j.vaccine.2022.10.006
7. Wise J. Microneedle patch for flu vaccination proves successful in human clinical trial. *BMJ*. 2017;j3120. doi:10.1136/bmj.j3120
8. Nuwarda RF, Alharbi AA, Kayser V. An overview of influenza viruses and vaccines. *Vaccines*. 2021;9(9):1032. doi:10.3390/vaccines9091032
9. Cox RJ. Correlates of protection to influenza virus, where do we go from here? *Hum Vaccin Immunother*. 2013;9(2):405–408. doi:10.4161/hv.22908
10. Esposito S, Montinaro V, Groppali E, et al. Live attenuated intranasal influenza vaccine. *Hum Vaccin Immunother*. 2012;8(1):76–80. doi:10.4161/hv.8.1.18809

11. Trombetta CM, Gianchecchi E, Montomoli E. Influenza vaccines: evaluation of the safety profile. *Hum Vaccin Immunother*. 2018;14(3):657–670. doi:10.1016/j.vaccine.2017.08.088
12. Sia ZR, Miller MS, Lovell JF. Engineered nanoparticle applications for recombinant influenza vaccines. *mol Pharm*. 2021;18(2):576–592. doi:10.1021/acs.molpharmaceut.0c00383
13. Hendy DA, Amouzougan EA, Young IC, et al. Nano/microparticle formulations for universal influenza vaccines. *AAPS J*. 2022;24(1):24. doi:10.1208/s12248-021-00676-9
14. Qiao D, Liu L, Chen Y, et al. Potency of a scalable nanoparticulate subunit vaccine. *Nano Lett*. 2018;18(5):3007–3016. doi:10.1021/acs.nanolett.8b00478
15. Franchi L, Warner N, Viani K, et al. Function of nod-like receptors in microbial recognition and host defense. *Immunol Rev*. 2009;227(1):106–128. doi:10.1111/j.1600-065X.2008.00734.x
16. Griffiths PC, Cattoz B, Ibrahim MS, et al. Probing the interaction of nanoparticles with mucin for drug delivery applications using dynamic light scattering. *Eur J Pharm Biopharm*. 2015;97(Pt A):218–222. doi:10.1016/j.ejpb.2015.05.004
17. Xiu X, Gao G, Liu Y, et al. Drug delivery with dissolving microneedles: skin puncture, its influencing factors and improvement strategies. *J Drug Delivery Sci Technol*. 2022;76:103653. doi:10.1016/j.jddst.2022.103653
18. Su R, Zhang R, Wang Y, et al. Simulated skin model for in vitro evaluation of insertion performance of microneedles: design, development, and application verification. *Comput Methods Biomech Biomed Engin*. 2024:1–10. doi:10.1080/10255842.2024.2372621
19. Williams MS. Single-radial-immunodiffusion as an in vitro potency assay for human inactivated viral vaccines. *Vet Microbiol*. 1993;37(3–4):253–-262. doi:10.1016/0378-1135(93)90027-5
20. Huang Y, Lin Z, Wang W, et al. Comparison of hemagglutination inhibition and hemagglutinin pseudovirus neutralization titres in relation to protection against influenza in a mouse model. *Lett Appl Microbiol*. 2021;73(3):294–299. doi:10.1111/lam.13513
21. Xie Y, Peng C, Gao Y, et al. Mannose-based graft polyesters with tunable binding affinity to concanavalin A. *J Polym Sci Part A*. 2017;55(23):3908–3917. doi:10.1002/pola.28776
22. Fan Y, Moon JJ. Particulate delivery systems for vaccination against bioterrorism agents and emerging infectious pathogens. *Wiley Interdiscip Rev Nanomed Nanobiotechnol*. 2017;9(1). doi:10.1002/wnan.1403
23. Mant A, Chinnery F, Elliott T, et al. The pathway of cross-presentation is influenced by the particle size of phagocytosed antigen. *Immunology*. 2012;136(2):163–175. doi:10.1111/j.1365-2567.2012.03558.x
24. Xiu X, Ma S, Li Z, et al. Novel 3D integrated microfluidic device: design, construction, and application to the preparation of liposomes for vaccine delivery. *J Drug Delivery Sci Technol*. 2024;91:105191. doi:10.1016/j.jddst.2023.105191
25. Zhao J, Li J, Jiang Z, et al. Chitosan,N,N, N-trimethyl chitosan (TMC) and 2-hydroxypropyltrimethyl ammonium chloride chitosan (HTCC): the potential immune adjuvants and nano carriers. *Int J Biol Macromol*. 2020;154:339–348. doi:10.1016/j.ijbiomac.2020.03.065
26. Ganbold T, Baigude H. Design of mannose-functionalized curdlan nanoparticles for macrophage-targeted siRNA delivery. *ACS Appl Mater Interfaces*. 2018;10(17):14463–14474. doi:10.1021/acsami.8b02073
27. Chen S, Yang L, Ou X, et al. A new polysaccharide platform constructs self-adjuvant nanovaccines to enhance immune responses. *J Nanobiotechnology*. 2022;20(1):320. doi:10.1186/s12951-022-01533-3
28. Liu L, Ma P, Wang H, et al. Immune responses to vaccines delivered by encapsulation into and/or adsorption onto cationic lipid-PLGA hybrid nanoparticles. *J Control Release*. 2016;225:230–239. doi:10.1016/j.jconrel.2016.01.050
29. Jaudzems K, Kirsteina A, Schubeis T, et al. Structural analysis of an antigen chemically coupled on virus-like particles in vaccine formulation. *Angew Chem Int Ed Engl*. 2021;60(23):12847–12851. doi:10.1002/anie.202013189
30. Nanda KK, Maisels A, Kruis FE, et al. Higher surface energy of free nanoparticles. *Phys Rev Lett*. 2003;91(10):106102. doi:10.1103/PhysRevLett.91.106102
31. Wang Q, Wang Z, Sun X, et al. Lymph node-targeting nanovaccines for cancer immunotherapy. *J Control Release*. 2022;351:102–122. doi:10.1016/j.jconrel.2022.09.015
32. Dukhin SS, Labib ME. Convective diffusion of nanoparticles from the epithelial barrier toward regional lymph nodes. *Adv Colloid Interface Sci*. 2013;199:23–43. doi:10.1016/j.cis.2013.06.002
33. Li X, Xiu X, Su R, et al. Immune cell receptor-specific nanoparticles as a potent adjuvant for nasal split influenza vaccine delivery. *Nanotechnology*. 2024;35(12). doi:10.1088/1361-6528/ad1644
34. Cummings RD. The mannose receptor ligands and the macrophage glycome. *Curr Opin Struct Biol*. 2022;75:102394. doi:10.1016/j.sbi.2022.102394
35. Jin Z, Li W, Cao H, et al. Antimicrobial activity and cytotoxicity of N-2-HACC and characterization of nanoparticles with N-2-HACC and CMC as a vaccine carrier. *Chem Eng J*. 2013;1(221):331–341. doi:10.1016/j.cej.2013.02.011
36. Jin Z, Hu G, Zhao K. Mannose-anchored quaternized chitosan/thiolated carboxymethyl chitosan composite NPs as mucoadhesive carrier for drug delivery. *Carbohydr Polym*. 2022;283:119174. doi:10.1016/j.carbpol.2022.119174
37. Du X-J, Wang J-L, Iqbal S, et al. The effect of surface charge on oral absorption of polymeric nanoparticles. *Biomater Sci*. 2018;6(3):642–650. doi:10.1039/c7bm01096f
38. Lan X, She J, Lin D-A, et al. Microneedle-mediated delivery of lipid-coated cisplatin nanoparticles for efficient and safe cancer therapy. *ACS Appl Mater Interfaces*. 2018;10(39):33060–33069. doi:10.1021/acsami.8b12926
39. Schepens B, Vos PJ, Saelens X, van der Maaden K. Vaccination with influenza hemagglutinin-loaded ceramic nanoporous microneedle arrays induces protective immune responses. *Eur J Pharm Biopharm*. 2019;136:259–266. doi:10.1016/j.ejpb.2019.02.002
40. Bao Y, Liu Z, Liu Y, Ma F. Preparation and characterization of dissolving microneedles with nano-enhanced mechanical properties. *Acta Pharma Sin*. 2021;56(7):1999–2004. doi:10.16438/j.0513-4870.2021-0222
41. Gao H, Gonçalves C, Gallego T, et al. Comparative binding and uptake of liposomes decorated with mannose oligosaccharides by cells expressing the mannose receptor or DC-SIGN. *Carbohydr Res*. 2020;487:107877. doi:10.1016/j.carres.2019.107877
42. Hardy S, Eichelberger M, Griffiths E, et al. Confronting the next pandemic—workshop on lessons learned from potency testing of pandemic (H1N1) 2009 influenza vaccines and considerations for future potency tests, Ottawa, Canada, July 27–29, 2010. 2011. doi:10.1111/j.1750-2659.2011.00250.x

43. Dunn A, Duffy C, Gordon A, et al. Comparison of single radial immunodiffusion and ELISA for the quantification of immunoglobulin G in bovine colostrum, milk and calf sera[J]. *J Appl Animal Res*. 2018;46(1):758–765. doi:10.1080/09712119.2017.1394860
44. Mould RC, AuYeung AW, van Vloten JP, et al. Enhancing immune responses to cancer vaccines using multi-site injections. *Sci Rep*. 2017;7(1):8322. doi:10.1038/s41598-017-08665-9
45. Madhusudana SN, Anand NP, Shamsundar R. Economical multi-site intradermal regimen with purified chick embryo cell vaccine (Rabipur) prevents rabies in people bitten by confirmed rabid animals. *Inter J Infect Dis*. 2002;6(3):210–214. doi:10.1016/S1201-9712(02)90113-X